Massive Dirac fermions and strong Shubnikov–de Haas oscillations in single crystals of the topological insulator Bi_2Se_3 doped with Sm and Fe

Weiyao Zhao,[1,2,*] Chi Xuan Trang,[3] Qile Li,[3] Lei Chen,[1] Zengji Yue,[1,2] Abuduliken Bake,[1] Cheng Tan,[4] Lan Wang,[4] Mitchell Nancarrow,[1] Mark Edmonds,[3,†] David Cortie,[1,2] and Xiaolin Wang[1,2,‡]

[1]*Institute for Superconducting and Electronic Materials, Australian Institute for Innovative Materials, University of Wollongong, Wollongong, New South Wales 2500, Australia*

[2]*ARC Centre of Excellence in Future Low-Energy Electronics Technologies FLEET, University of Wollongong, Wollongong, New South Wales 2500, Australia*

[3]*School of Physics & Astronomy, & ARC Centre of Excellence in Future Low-Energy Electronics Technologies FLEET, Monash University, Clayton, Victoria 3800, Australia*

[4]*School of Science, RMIT University, Melbourne, Victoria 3001, Australia*

(Received 18 February 2021; accepted 16 August 2021; published 30 August 2021)

Topological insulators (TIs) are emergent materials with unique band structure, which allow the study of quantum effect in solids, as well as contribute to high-performance quantum devices. To achieve the better performance of TIs, here, we present a codoping strategy using synergistic rare-earth (RE) Sm and transition-metal Fe dopants in Bi_2Se_3 single crystals, which combine the advantages of both a transition-metal-doped TI [high ferromagnetic ordering temperature and observed quantum anomalous Hall effect (QAHE)], and a RE doped TI (large magnetic moments and significant spin-orbit coupling). In the as-grown single crystals, clear evidences of ferromagnetic ordering were observed. The angle-resolve photoemission spectroscopy indicates the ferromagnetism opens a ∼44 meV band gap at the surface Dirac point. Moreover, the mobility of the carriers at 3 K is ∼7400 cm^2/Vs, and we thus observed an ultra-strong Shubnikov–de Haas oscillation in the longitudinal resistivity, as well as the Hall steps in transverse resistivity <14 T. Our transport and angular-resolved photoemission spectroscopy results suggest that the RE and transition metal codoping in the Bi_2Se_3 system is a promising avenue to implement the QAHE, as well as harnessing the massive Dirac fermion in electrical devices.

DOI: 10.1103/PhysRevB.104.085153

I. INTRODUCTION

Topological insulators (TIs) are materials with insulating bulk states and robust conducting edge modes protected by time-reversal symmetry and offer opportunities for spintronics, non-Abelian quantum computing, and energy-efficient electronic devices. Intrinsic TIs are usually nonmagnetic materials possessing linear dispersed surface states (SSs) with helical-textured spin configuration [1–4]. Magnetism has been identified to be a useful control parameter in TIs because the spin degree of freedom introduces a perturbation that can break time-reversal symmetry, opening channels for backscattering, generating axion electrodynamics [5], and opening a gap at Dirac cones SSs [6,7]. A special case occurs when ferromagnetic order in a TI system induces a zero magnetic field quantized Hall resistance response: the quantum anomalous Hall effect (QAHE). To obtain the QAHE state, two critical conditions have to be simultaneously satisfied [6]: (1) Long-range ferromagnetic order must give rise to an out-of-plane magnetization to gap the Dirac cone, and (2) the Fermi energy of the system must stay in both bulk and surface gaps. Chen *et al.* [6] demonstrated that Mn or Fe dopants can open a gap in the SSs in Bi_2Se_3, e.g., ∼44 meV by 12% Fe doping, ∼50 meV by 16% Fe doping, and ∼7 meV by 1% Mn doping. In their experiments, higher Fe doping concentrations resulted in stronger ferromagnetism and therefore a larger surface gap; however, the Fermi energy E_f is nearly constant with the Fe level [6]. In contrast, the Mn dopant shifts E_f to both (bulk and surface) band gaps effectively, e.g., in 1% Mn level, the E_f is shifted ∼160 meV down into the band gaps; however, the limited concentration of dopants also limits the effective ferromagnetic moments, as well as the Dirac gap width [6]. Zhang *et al.* [8,9] found that, in a fine-tuned Cr-doped $Bi_{0.2}Sb_{1.8}Te_3$ thin film, the quantized Hall resistivity h/e^2 (where e is the charge of electron, and h is the Planck's constant) can be observed at zero magnetic field, concurrent with a vanishing longitudinal resistance. Angle-resolved photoelectron spectroscopy (ARPES) results [10] indicated that, in the latter samples, the E_f is around the Dirac point, and Cr dopants open a gap on the Dirac cone. Building on this success, the transition metal dopants, like V, Cr, Mn, and Fe, have generally emerged as the most popular building blocks for long-range ferromagnetic ordering in TIs [6,8,9,11,12]. However, the drawback is that a relatively high doping level is needed to open a large enough surface Dirac gap, which

*wz929@uowmail.edu.au
†mark.edmonds@monash.edu
‡xiaolin@uow.edu.au

also decreases the mobility of the carriers in TIs and, in some cases, introduces in-gap defect band states [8,13].

Compared with transition metal dopants, the magnetism of rare-earth (RE) dopants in TIs are significantly different. RE ions typically have larger moments owing to their unpaired $4f$ electrons, unquenched orbital magnetic moment, and high spin-orbit coupling. However, the localized nature of $4f$ electrons generally prohibits strong direct magnetic exchange and gives rise to low Curie temperatures [14–16]. Van Vleck [17], or itinerant electron exchange [18], or Dirac-mediated Ruderman-Kittel-Kasuya-Yosida (RKKY) coupling [19] can potentially enhance ordering temperatures in RE TIs. To date, however, a high-temperature TI using RE dopants has been elusive. Nevertheless, several other properties of the RE-doped TIs are attractive. For example, in Sm-doped Bi_2Se_3 [20], the ferromagnetism originates at a relatively low doping level, where the mobility of the carriers is still high ($7200\,cm^2/Vs$ for 2.5% Sm doping). More importantly, we notice that, in the density functional theory (DFT) calculations on Sm-doped Bi_2Se_3 [20], the carriers near E_f are fully spin polarized, demonstrating an ultrahigh mobility of half metallic states (comparing with existing half metals: EuO [21] $\sim 50\,cm^2/Vs$ and CrO_2 [22] $5\,cm^2/Vs$). However, the tradeoff from Sm doping is that the E_f penetrates deeply into the bulk conducting bands and therefore resulting in bulk-dominant transport behaviors [20].

Based on the advantages and disadvantages of transition metal or RE doping in TI, here, we propose a strategy to explore codoping of RE and transition metals to search for synergistic effects. We believe that, in this system, the low-level dopants can introduce ferromagnetism, as well as keep their high mobility and close-to-gaps Fermi energy. In this paper, we report that Sm and Fe can be dual doped in a Bi_2Se_3 single crystal (SFBS), with a relatively low concentration (both $\sim$2% experimentally). The dopants successfully introduce ferromagnetism into Bi_2Se_3, with high ordering temperature ($\sim$30 K bulk Sm-Fe, $>$250 K Fe impurities), and keep their high mobility of $\sim 7400\,cm^2/Vs$ at 3 K. More importantly, our ARPES results prove that the Dirac cone of the SSs has opened a gap of $\sim$44 meV (like 12% Fe doping). In tandem, magnetotransport experiments show the ultra-strong Shubnikov–de Haas (SdH) oscillations with a nontrivial Berry phase, as well as steplike behavior in Hall effect curves. Angle-dependent measurements suggest the strong anisotropic Fermi surface in the crystals. The properties we report in Sm and Fe dual doped Bi_2Se_3 crystal indicate that it is a strong candidate to achieve QAHE, and more generally, codoping RE and transition metal dopants is a promising scheme in TI materials.

II. EXPERIMENTS

A. Single crystal growth

We employed a simple melting-cooling method in a uniform-temperature vertical furnace to spontaneously crystallize the raw elements into a tetradymite structure ($Sm_{0.02}Fe_{0.02}Bi_{1.96}Se_3$, SFBS). Briefly, high-purity Sm, Bi, Fe, and Se powders ($\sim$6 g) were mixed and sealed in a quartz tube as starting materials. The crystal growth was carried out using the following procedure: (i) heating of the mixed powders to completely melt them; (ii) maintaining this temperature for 24 h to ensure that the melt was uniform; and (iii) slowly cooling the melt down to 500 °C to crystallize the sample. Since the Fe and Sm dopants possess a higher melting point, in steps (i) and (ii), we set the melting temperature at 1100 °C to ensure the molten elements interacted in the liquid state. After growth, single crystal flakes with a typical size of $3 \times 3 \times 0.3\,mm^3$ could be easily exfoliated mechanically from the ingot. The single crystals prefer to naturally cleave along the (001) direction, resulting in the c axis being the normal direction of these flakes, as is commonly the case in this family of materials. The dopant distribution of SFBS was confirmed using scanning electron microscopy (SEM), and energy x-ray dispersive spectroscopy (EDS).

B. Transport and magnetic measurements

The electronic transport properties were measured using a physical properties measurement system (PPMS-14T, Quantum Design). Hall bar contact measurements were performed on a freshly cleaved c-plane crystal, using silver paste cured at room temperature. The electric current was parallel to the c plane, while the magnetic field was perpendicular to the c plane. The angle dependence of the magnetoresistance (MR) was also measured using a horizontal rotational rig mounted on the PPMS. During rotation, the sample alignment was chosen such that the magnetic field was always perpendicular to the electronic current. The vibration sample magnetometer module on the PPMS was employed to conduct the magnetic measurements. In zero-field-cooled (ZFC) mode, the sample was cooled to 3 K at zero fields, followed by magnetization measurements during heating up with a small measuring field (500 Oe). In field-cooled (FC) mode, a 500 Oe magnetic field was added during cooling down to 3 K, and the sample was measured upon heating in the 500 Oe field. Hysteresis loops were also measured at different temperatures to track the coercive field and field-dependent magnetic susceptibility.

C. ARPES

The ARPES measurements were performed at Beamline 10.0.1 of the Advanced Light Source (ALS) at Lawrence Berkeley National Laboratory, USA. Samples were mounted on a holder using conductive epoxy with a cleaving post, which was removed in ultrahigh vacuum at low temperature to yield a pristine surface for ARPES measurements. Data were taken using a Scienta R4000 analyzer at 20 K with s-polarized light. The total convolved energy resolution was 15 meV, and angular resolution was 0.2 °, resulting in an overall momentum resolution of $\sim 0.01\,Å^{-1}$ for photoelectron kinetic energies measured.

D. DFT calculations

DFT calculations were carried out using the plane-wave code Vienna *Ab initio* Simulation Package (VASP) version 5.44 [23]. The generalized gradient approximation (GGA) using the Perdew-Burke-Ernzerhof exchange-correlation functional was employed, together with the spin-orbit interaction and Hubbard correction for the Fe $3d$ levels with $U = 4$ and

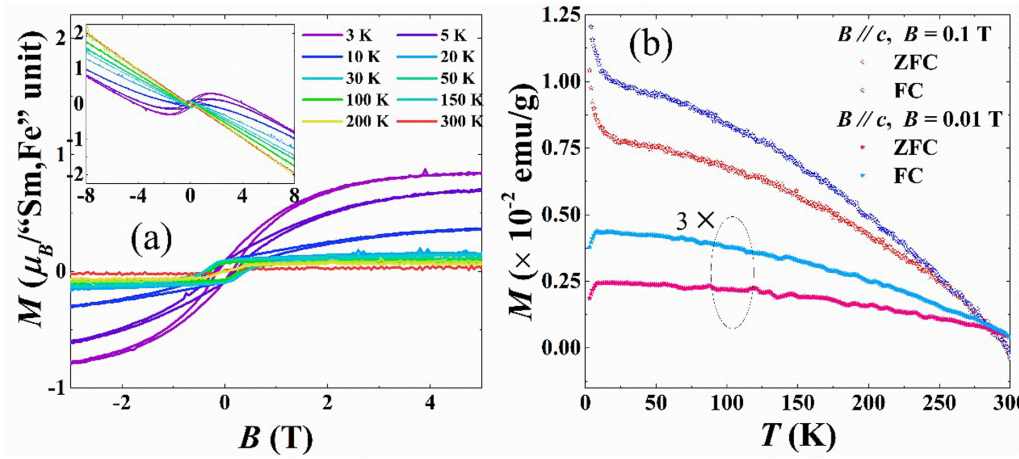

FIG. 1. The magnetic properties of Sm and Fe dual doped Bi_2Se_3 single crystal flake. (a) The hysteresis loops measured at certain temperatures from 3 to 300 K, obtained via subtracting the diamagnetic background of original magnetic hysteresis curves [shown in the inset of (a)]. Note that the magnetization values are shown in moment of a "SmFe" unit. (b) The temperature-dependent magnetization from 3 to 300 K at different applied magnetic fields. Note that the magnetization values of 0.01 T data are plotted in three times to show the details.

$J = 1$ eV implemented using the rotationally invariant method developed by Liechtenstein [24]. Both pure Bi_2Se_3 and SFBS were simulated with identical levels of precision. To simulate low doping, $3 \times 3 \times 2$ supercells were constructed containing 58 atoms. To mitigate the complexity of the Sm $4f$ electrons, which are a known deficiency of DFT, we employed the frozen core approach based on a custom projector augmented wave pseudopotential. The lowest energy states of the Fe and Sm dopants were identified by simulating different configurations and interseparation and performing ionic relaxation. These were compared with the alternate calculations treating the Sm $4f$ as valence including a Hubbard correction with $U = 6$ eV and $J = 1$ eV. The plane-wave energy cutoff was 500 eV, and forces were converged to better than 0.01 eV/Å.

III. RESULTS AND DISCUSSION

A. Ferromagnetism

As the most important feature of magnetic ion-doped TIs, the magnetic ordering in SFBS has been studied. The applied magnetic field and temperature-dependent magnetization behavior are shown in Fig. 1. As shown in Fig. 1(a), the hysteresis loops (magnetic hysteresis curves) at various temperatures from 3 to 300 K of SFBS exhibit clear signs of ferromagnetic ordering, in which the total magnetization was converted from the emu/g to Bohr magneton per "SmFe" unit. Note that, in Fig. 1(a), the raw diamagnetic background was subtracted from the original data [the inset of Fig. 1(a)] to exhibit the "pure" loop. The saturation moment is large by the standard of a dilute magnetic semiconducting system approaching $1\,\mu_B$ per Sm-Fe pair. This is, however, less than expected for a fully aligned $Sm^{3+}(4f^5, S = \frac{5}{2}, L = 5, J = \frac{5}{2})$ and $Fe^{3+}(3d^5, S = \frac{5}{2}, L = 0, J = \frac{5}{2})$ which would be $\sim 6\,\mu_B$ for a ferromagnetic collinearly aligned Sm^{3+}–Fe^{3+} spin dimer. Instead, this implies that either only a fraction of the Sm^{3+} and Fe^{3+} contribute magnetically, or more likely, the Sm^{3+} and Fe^{3+} are in a noncollinear ferrimagnetic arrangement. Noncollinear spin arrangements are favored by the Dzyaloshinskii-Moriya interaction, owing to the strong spin-orbit effects in TIs. Below ~10 K, the loop shape is a slim S shape with low coercive field, which is often a hallmark of complex spin structure, or the ferrimagnet nears its compensation point. With heating up, the system transitions smoothly to a state with a higher coercive field, giving a quasisquare shape typical of a simpler ferromagnet; however, the saturation moment per "SmFe" unit decreases to $\sim 0.1\,\mu_B$. We attribute this to Fe forming the dominant magnetic sublattice at higher temperatures, where the Sm is paramagnetic. Further, we measured the temperature-dependent magnetization curves in both ZFC and FC procedures between 3 and 300 K, as shown in the Fig. 1(b), with 100 and 1000 Oe applied magnetic field. One can see the clear difference of the ZFC and FC curves at ~250 and ~270 K, at different applied fields, which indicate history dependence to magnetize that is a hallmark of a magnetically ordered state, as such paramagnetic materials do not typically show hysteresis at such high temperatures. This suggests that ferromagnetism or ferrimagnetism may be present in the crystals, and this is attributed to the ordering of Fe moments, either within the bulk of the crystal or on the surface itself. Below the ordering temperature of Fe, the magnetization increases monotonically with cooling down, which is due to the increasing effective moment of the Fe^{3+} below its Curie temperature. However, something dramatic occurs below ~30 K, where the magnetization increases suddenly with further cooling. This is attributed to the effect of larger Sm^{3+} moments that begin to play a significant role.

B. DFT

During DFT calculation, the Fe and Sm were placed in variable locations of the supercell to identify the lowest-energy configuration of the Sm-Fe defect pair. Nearest neighbor and next-nearest neighbor Sm-Fe configurations are energetically unfavorable, and the minimal energy state was found for the Sm and Fe at the maximal distance of 10.78 Å, resulting in the structure and spin electron density shown in Fig. 2(a). The nearest neighbor configuration was strongly

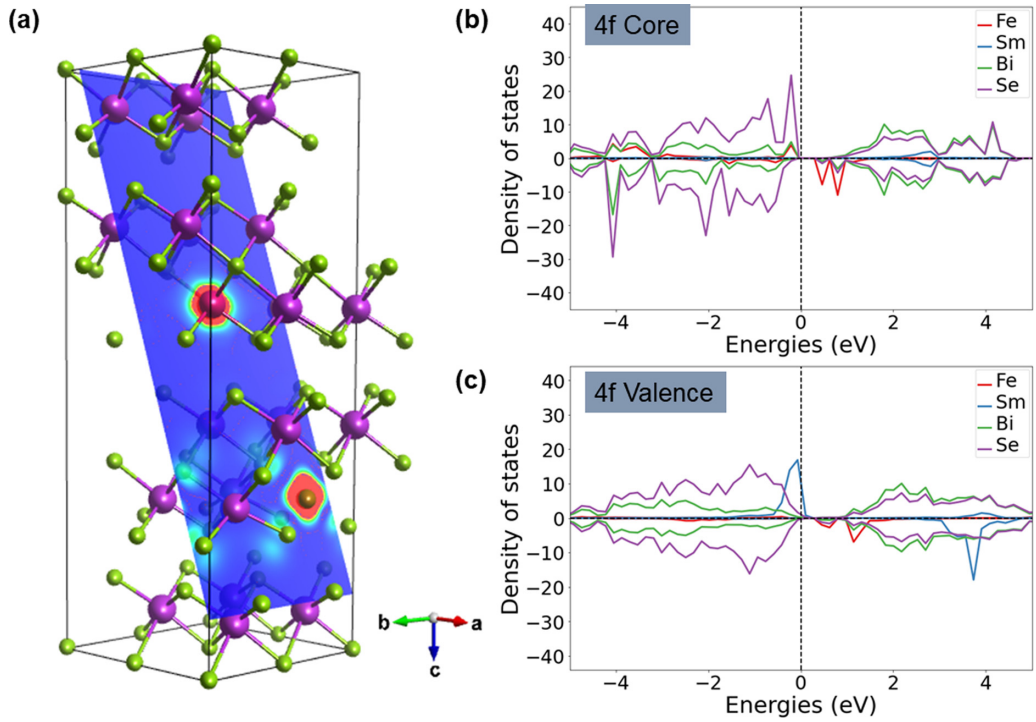

FIG. 2. Density functional theory (DFT) calculations for SFBS. (a) The chemical structure is shown for a supercell containing isolated Sm and Fe defects, superimposed with the spin difference electron density within a $(10\bar{1})$ plane. Both Sm and Fe carry large magnetic moments (red), where fainter induced moments appear on the Se atoms coordinating the Fe. (b) The partial electronic density of states (PDOS) for the frozen $4f$-core calculation shows a high degree of spin polarization at the Fermi level. (b) The PDOS for the GGA + U $4f$ valence calculation also indicates a similar half-metallic character.

disfavored by 700 meV because this involves significant distortions of the Sm-Se octahedra involving bond stretching introduced by the presence of the smaller iron atom nearby. Overall, the alternative solutions with Fe and Sm further apart (at least 6 Å) were energetically favorable, indicating that the clustering of Fe and Sm into biatom defects is unlikely in this system. Large spin magnetic moments of 5.5 and 3.6 μ_B were found on the Sm and Fe sites respectively, indicating the strong intrinsic magnetism for the $4f$ and $3d$ dopants, respectively. This leads to strong exchange splitting and spin polarization in the electron structure. The partial electronic density of states (PDOS) is shown in Figs. 2(b) and 2(c), which used the frozen core and the GGA + U method, respectively. The two spin-polarized densities of state are shown simultaneously, where opposite spin states are mirrored across the x axis. In both cases, the bands near the Fermi level are fully spin polarized, indicating that this system is nearly an ideal half-metal. However, the calculations that treat the $4f$ electrons as valence electrons using the GGA + U approach predict a higher density of narrow-band states appear at the valence band (VB) maximum, which manifests as flat bands spanning the Fermi surface. Past calculations of Sm:Bi_2Se_3 have predicted similar half-metallic features [20].

IV. ARPES MEASUREMENTS

We now turn to ARPES to examine the electronic band structure of SFBS to determine whether the topological SS is preserved and whether a gap in the SS has opened due to the magnetic dopants breaking time-reversal symmetry. The addition of dopants may also alter the size of the bulk band gap in three-dimensional (3D) TI's [11,25]. In an ARPES measurement on 3D TIs, it is crucial to be able to distinguish between bulk bands and SS bands. A SS possesses entirely in-plane electron momentum ($k_{||}$), which can be determined by the momentum conservation of photoelectrons given by $k_{||} = \sqrt{\frac{2m_e}{\hbar^2}E_k \sin^2\theta}$, where E_k is the kinetic energy of the emitted photoelectron, and θ is the emission angle. In contrast, determining the bulk band dispersion (i.e., the out-of-plane momentum component k_z) requires a series of photon energy-dependent ARPES measurements to be performed. From these measurements, the nearly free-electron final state approximation can be used to derive k_z [26–28] and is given by $k_z = \sqrt{\frac{2m_e}{\hbar^2}(E_k + V_0) - k_{||}^2}$, where V_0 is a potential parameter describing the separation between the vacuum level and bottom of the VB. At normal emission ($\theta = 0$), this expression reduces to $k_z = \sqrt{\frac{2m_e}{\hbar^2}(E_k + V_0)}$.

To evaluate the bulk band gap in SFBS, we have performed photon energy-dependent ARPES measurements and extracted energy distribution curves (EDCs) at the Γ point to determine E_B vs k_z. In Fig. 3(a), we plot binding energy E_B as a function of $h\nu$ in the upper horizontal scale, which is then converted to wave vector k_z in the bottom horizontal scale using the nearly free-electron final state model. It is clear there is a marked dispersion in both the bulk VB and bulk conduction band (CB), and they reach maxima and minima, respectively, at a photon energy of $h\nu = 60$ eV, as displayed in Fig. 3(b). From these ARPES spectra, it is clear the overall

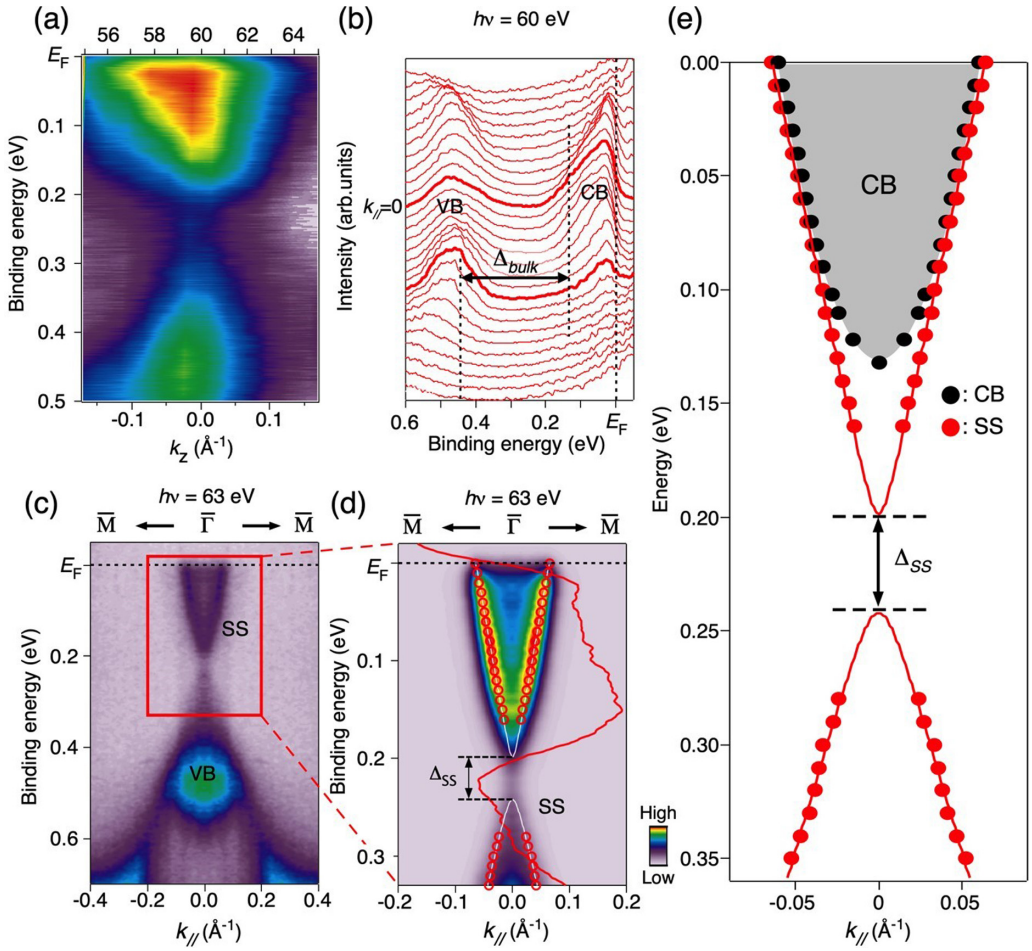

FIG. 3. Angle-resolved photoelectron spectroscopy (ARPES) study of SFBS. (a) Photon-energy dependence of the normal-emission ARPES intensity near E_F as a function of wave vector along the z direction with corresponding photon energies on top. (b) Energy distribution curves measured with $h\nu = 60$ eV, allowing determination of the conduction band (CB) minimum and valence band (VB) maximum. (c) ARPES intensity measured with $h\nu = 63$ eV around the $\bar{\Gamma}$ point. (d) High-resolution data of (c) but focused on the near-E_F region. (e) Intensity maxima of ARPES spectra, measured from peak maxima of momentum distribution curves of CB (black) and surface state (SS; red).

CB and VB structure displays the same characteristic features of pristine Bi_2Se_3, as well as a similar overall band gap which we determine to be ∼310 meV for SFBS. This suggests Fe and Sm dopants cause minimal change to the overall bulk band structure. To highlight the intensity of the SS features, ARPES measurements along the Γ-M high-symmetry direction at $h\nu = 63$ eV were performed, shown in Fig. 3(c). It is immediately clear the characteristic Dirac SS of a 3D TI is present between E_F to ∼0.4 eV below E_F. The linear dispersion of the electron and hole bands of the Dirac cone away from the Dirac point region possess Fermi velocities 5×10^5 and 3.9×10^5 ms^{-1}, respectively, consistent with the topological SS of pristine Bi_2Se_3 [29]. We can also extract the Fermi vector $k_F \sim 0.06$ Å^{-1}.

Time-reversal symmetry protection of the Dirac point is well known to be broken by magnetic dopants [6,7,30], leading to a gap opening in the SS. To investigate this, we performed high-resolution ARPES measurements near E_F [Fig. 3(d)] at 20 K. In the Dirac point region (∼0.21 eV below E_F), we did not observe a completely suppressed intensity region that can be immediately attributed to a band gap opening. This may be explained from the magnetic property measurements in Fig. 1, which demonstrate that 20 K is on the cusp of full magnetic ordering. Thus, at 20 K in the ARPES measurements, not all magnetic dopant spins are aligned, leading to the appearance of some spectral weight in the gapped region. However, the pronounced minima in intensity from the EDC [red overlay curve in Fig. 3(d)] suggest the presence of a small gap rather than a discrete Dirac point.

To examine this band gap, we first extract momentum distribution curves from the ARPES spectra, and we fit the data to a model of a massive Dirac dispersion given by

$$E_i(k) = D \pm \sqrt{\Delta_i^2 + \hbar^2 v_{F,i}^2 (k + k_0)^2}, \quad i \in n, p, \qquad (1)$$

where $\Delta = \Delta_n + \Delta_p$ represents the band gap, D the doping, and $v_{F,i}$ the asymptotic Fermi velocities away from the gapped region at large momenta. Using the determined Fermi velocities obtained away from the gapped region, we then fit the ARPES spectra using the function in Eq. (1) to determine Δ_n and Δ_p and consequently the band gap Δ. This model is plotted as a white solid line in Fig. 3(d), yielding a magnetic gap of 44 ± 15 meV, consistent with the gap size of 12%

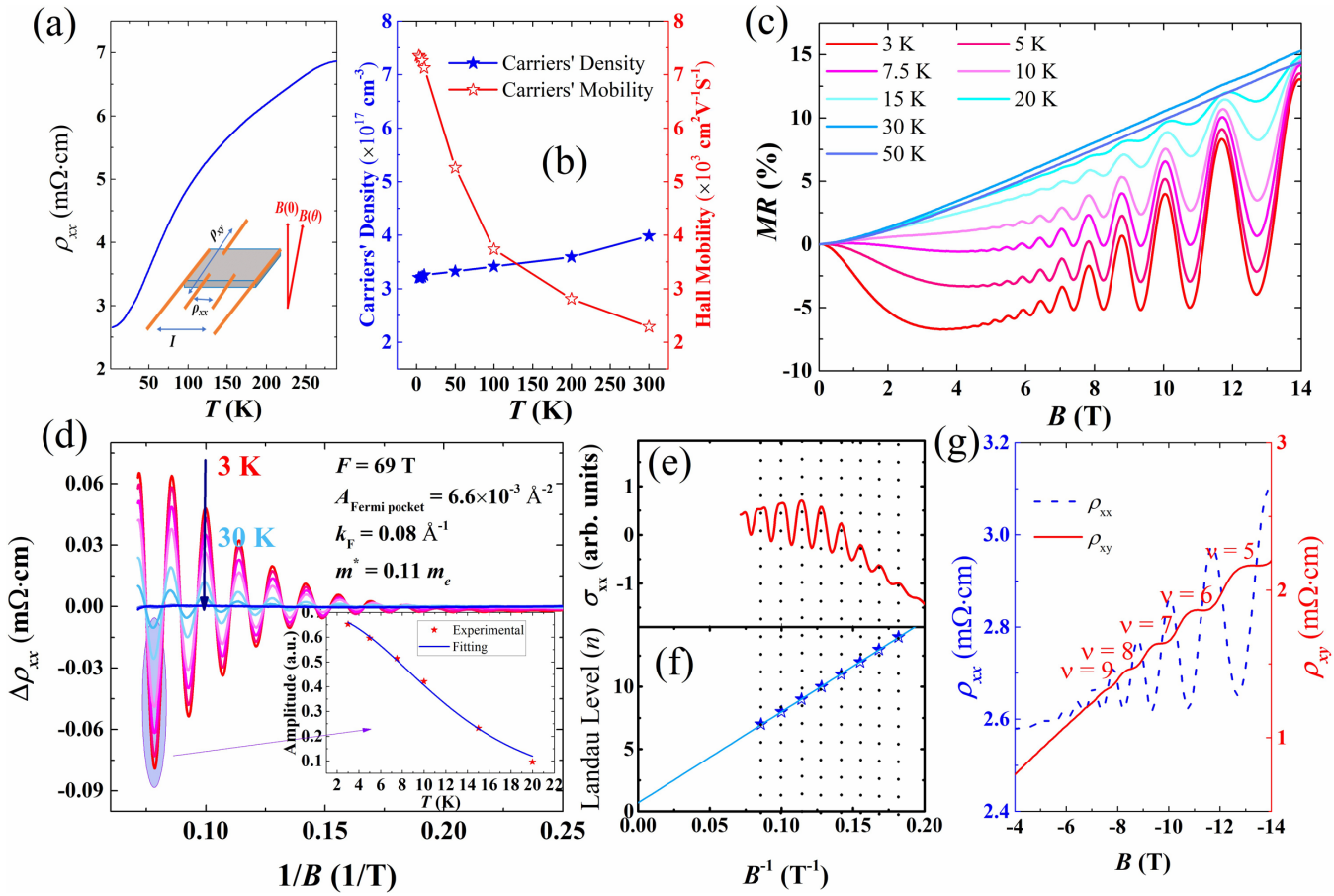

FIG. 4. Transport properties of SFBS single crystal. (a) The temperature-dependent resistivity of SFBS single crystal. Inset: A sketch of the measurement configurations. (b) Calculated density and mobility of carriers as a function of temperature extracted from the Hall and resistivity measurements. (c) The magnetoresistance (MR) of SFBS single crystal, displaying ultra-strong Shubnikov–de Haas (SdH) oscillations. (d) The pure SdH oscillation patterns obtained from MR data after subtracting a continuous background term. Inset: Lifshitz-Kosevich (LK) formula fitting for effective mass. (e) The oscillation patterns in calculated longitudinal conductivity and (f) Landau fan diagram. (g) The zoom-in plot of 3 K Hall effect curve and MR curve in −4 to −14 T regime, in which the steplike effect can be found in the Hall effect curve.

Fe-doped Bi_2Se_3. The addition of dopants may also alter the size of the bulk band gap in 3D TIs [11,25].

Finally, we fit the CB [black points in Fig. 3(e)] to a nearly free-electron model $E = \frac{\hbar^2 k^2}{2m^*}$ within a 0.08 Å^{-1} region extending from the Γ point. The parabolic dispersion yields an effective mass of $m^* \sim 0.1 \pm 0.020 m_0$. This value is like the value of pristine Bi_2Se_3 [31]. Lastly, we plot in Fig. 3(e) the extracted CB [Fig. 3(b)] and SS band [Fig. 3(d)] dispersions to more clearly highlight the paraboliclike and linearlike dispersions.

A. MR and ultra-strong SdH oscillations

As illustrated by ARPES, the band structure of SFBS crystal is *n*-type metallic due to defects, such as Se vacancies. Therefore, in transport measurement, we observed similar metallic ground states in the plot of the temperature dependence of bulk resistivity [Fig. 4(a)]. The residual resistance ratio (*RRR*), defined by $RRR = \rho(300\,\mathrm{K})/\rho(3\,\mathrm{K})$ for the sample, is ∼2.5, which is comparable with pristine Bi_2Se_3 reported in past work [32]. The Hall effect measurements at various temperatures from 3 to 300 K show *n*-type features in the whole temperature range, as shown in Fig. S4 in the Supplemental Material [33]. The Hall curves are nearly linearlike between −14 and 14 T, and with steplike behavior at high magnetic field region, which we will discuss later. By fitting the Hall curves, we obtained the density of the carriers via $n = (R_H \cdot e)^{-1}$, where the R_H is the Hall coefficient, and e is the charge of an electron. Further, the mobility of the carriers can be obtained via $\mu_H = \sigma \cdot R_H$, where the σ is the conductivity, as shown in Fig. 4(b). The carrier's concentration in the SFBS single crystal is $\sim 3.2 \times 10^{17}$ cm^{-3} at low temperatures, which increases with heating slightly to $\sim 4 \times 10^{17}$ cm^{-3} at 300 K. Specifically, the carriers possess a very high mobility, e.g., $\sim 7.4 \times 10^3$ cm^2 V^{-1} s^{-1} at 3 K and $\sim 2.3 \times 10^3$ cm^2 V^{-1} s^{-1} at room temperature. To understand the magnetotransport effects that are the hallmark of topological effects, the MR ratio $\mathrm{MR} = [R(B) - R(0)]/R(0)$ was measured, as shown in Fig. 4(c). The MR values at 14 T are between 10 and 15% in the <50 K region, with two important features: (1) <10 K and 3 T, the MR values keep decreasing with increasing magnetic fields to minimum values, e.g., ∼7.5% at 3 K and 3 T, and (2) obvious oscillation patterns are found <30 K and >3 T region, denoted as SdH oscillations, which indicate Landau quantization. The negative MR in SFBS crystals is different from the MR behavior in Bi_2Se_3 and Sm-doped Bi_2Se_3, which

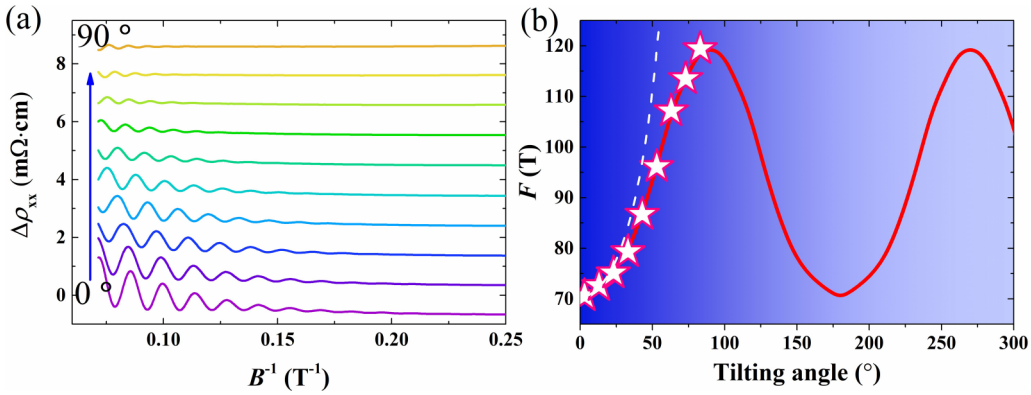

FIG. 5. The quantum oscillations in SFBS single crystals. (a) The angular dependence of Shubnikov–de Haas (SdH) oscillations, in which the oscillation frequencies are calculated and summarized in (b).

are shown in Figs. S5 and S6 in the Supplemental Material [33]. Since the negative MR effect in SFBS single crystal damps with heating dramatically and vanishes at ∼10 K, and this correlates with the onset of magnetic order with a high magnetization [as shown in Fig. 1(a)], we assign Sm^{3+} ordering to be the mechanism for this distinctive negative MR.

The SdH oscillations contain key information about the electronic structure, and these can be more easily interpreted by subtracting a smooth background to remove the MR contribution, as plotted in Fig. 4(c). It is apparent that the oscillations are much stronger than the SdH oscillations in other TIs, including our own work [13], so that the MR values are mainly contributed by the oscillations part, especially at 3–10 K. The amplitude of the oscillations is enhanced by the high mobility of carriers, as well as the negative MR contribution from magnetic dopants, which act to partially cancel the positive MR contributions. The SdH oscillations for a metal can be described by the Lifshitz-Kosevich (LK) formula, with a Berry phase included to account for the topological character of the system:

$$\frac{\Delta\rho}{\rho(0)} = \frac{5}{2}\left(\frac{B}{2F}\right)^{\frac{1}{2}} R_T R_D R_S \cos\left[2\pi\left(\frac{F}{B} + \gamma - \delta\right)\right], \quad (2)$$

where $R_T = \alpha T\nu/B\sinh(\alpha T\mu/B)$, $R_D = \exp(-\alpha T_D\nu/B)$, and $R_S = \cos(\alpha g\nu/2)$. Here, $\nu = m^*/m_0$ is the ratio of the effective cyclotron mass, m^* is the free-electron mass m_0, g is the g factor, T_D is the Dingle temperature, and $\alpha = (2\pi^2 k_B m_0)/\hbar e$, where k_B is the Boltzmann's constant, $\hbar$ is the reduced Planck's constant, and e is the elementary charge. The oscillation of $\Delta\rho$ is described by the cosine term with a phase factor $\gamma - \delta$, in which $\gamma = \frac{1}{2} - \Phi_B/2$, where Φ_B is the Berry phase. From the LK formula, the effective mass of carriers contributing to the SdH effect can be obtained through fitting the temperature dependence of the oscillation amplitude to the thermal damping factor R_T. From the temperature-damping relationship, we obtain the effective masses for these crystals as $\sim 0.11\, m_0$, as shown in the inset of Fig. 4(d), which is in good agreement with ARPES results for the effective mass of the bulk state. During the effective mass fitting, we employed the normalized amplitudes of the strongest peak minimum at ∼12.5 T. The quantum relaxation time and quantum mobility can also be obtained by $\tau = \hbar/2\pi k_B T_D$ and $\mu = e\tau/m^*$, respectively. According to the Onsager-Lifshitz equation, the frequency of quantum oscillation $F = (\varphi_0/2\pi^2)A_F$, where A_F is the extremal area of the cross-section of the Fermi surface perpendicular to the magnetic field, and φ_0 is the magnetic flux quantum. The cross-sections related to the 69 T pockets are 6.6×10^{-4} Å^{-2}, and if one assumes the Fermi pocket is roughly circular, the equivalent Fermi vector of ∼0.08 Å^{-1} is obtained, which is very close to the Fermi vector observed in ARPES. Further interesting features in SFBS are the steps in the Hall effect curve at low temperature, as shown in Fig. 4(g). The famous quantum Hall effect also presents steps with resistance values of $\frac{h}{\nu e^2}$, where ν is a constant for νth Landau level. Recently, the 3D quantum Hall effect has been observed in $ZrTe_5$ [34], which could be a possible explanation to the "steplike" behavior. The step behavior in SFBS might be related to this interesting effect. The Berry phase can be obtained via the Landau fan diagram, which is shown in Fig. 4(f). Since $\rho_{xx} \sim \rho_{xy}$, it is not valid to simply assign the maxima or minima of the SdH oscillation to integer (n) Landau levels to fit the n vs $1/B$ gradient since these quantities are instead related to total magnetoconductivity σ_{xx} [35,36]. Thus, we calculate the magnetoconductivity from $\sigma_{xx} = \rho_{xx}/(\rho_{xx}^2 + \rho_{xy}^2)$, as shown in Fig. 4(d), and assign the local maxima to ν. As we obtained from Fig. 3(f), the intercept has a value of ∼0.7 for SFBS crystal. In SFBS crystals, the spin configuration pattern can be understood as a competition between the out-of-plane time-reversal symmetry breaking component and the in-plane helical component. Depending on the Fermi level, the Berry phase can be modified away from π (0.5), as theoretically predicted [37] and experimentally observed via ARPES [30].

To further understand the Fermi surface geometry, we performed angle-dependent SdH oscillation measurements. The angular dependence of the MR properties is shown in Fig. 5(a) for SFBS crystal. Note that, during rotation, the magnetic field is always perpendicular to the current to mitigate any possible influence of the angle between the magnetic field and the current. The rotation parameter θ is the angle between the c axis and the direction of the magnetic field. At higher tilt angles, the SdH oscillation amplitude drops significantly, as expected for a dominantly two-dimensional Fermi surface. However, the angular dependence of frequency does not follow the $1/\cos\theta$ (white dashed line), and a small residual oscillation

persists at 90° instead of zero, which is a signature of the 3D bulk Fermi surface and quite similar to past reports of Fe-doped TIs [13]. To assess the size of the Fermi surface cross-section, we calculated the oscillation frequencies, and these are summarized in the inset of Fig. 3(a). The line of best fit to the quantum oscillation frequencies follows the trend expected for an elliptical Fermi surface inclined to the basal plane, as is known to be the case in the chalcogenide TIs.

V. CONCLUSIONS

In this paper, we proposed a RE and transition metal dual doped TI. The single crystal quality and the uniformity of dopants were checked by SEM and EDS. In electronic transport measurements, the low density of the carriers 3×10^{17} to $4 \times 10^{17}\,\mathrm{cm}^{-3}$ and high mobility 2.3×10^{3} to $7.4 \times 10^{3}\,\mathrm{cm}^{2}\,\mathrm{V}^{-1}\,\mathrm{s}^{-1}$ were observed. With strong magnetic fields, the SdH oscillations at low temperatures are drastically strong, showing nontrival Berry's phase; meanwhile, the steps in the Hall effect curve are also observed. Magnetometry measurements reveal strong bulk ferromagnetic order involving Sm^{3+} moments <30 K, which opens a gap at the Dirac point of the topological SSs, verified by ARPES. Employing DFT calculations, the fully spin-polarized Fermi surface is predicted, indicating a half-metallic TI state in SFBS single crystals. Our results suggest that the RE and transition metal codoping in the Bi_2Se_3 system is a promising material for the QAHE, as well as an ideal system to achieve low-energy electronic devices.

ACKNOWLEDGMENTS

We acknowledge support from the ARC Professional Future Fellowship (No. FT130100778), No. DE180100314, No. DP130102956, No. DP170104116, No. DP170101467, and No. DE160101157, and ARC Centre of Excellence in Future Low-Energy Electronics Technologies No. CE170100039. W.Z. acknowledges the financial assistance of an AINSE PGRA scholarship. M.T.E., C.X.T., and Q.L. acknowledge travel funding provided by the International Synchrotron Access Program managed by the Australian Synchrotron, part of the Australian Nuclear Science and Technology Organisation, and funded by the Australian Government. This research used resources of the ALS, which is a Department of Energy Office of Science User Facility under Contract No. DE-AC02-05CH11231. This research was undertaken with the assistance of resources and services from the National Computational Infrastructure, which is supported by the Australian Government.

[1] D. Hsieh, D. Qian, L. Wray, Y. Xia, Y. S. Hor, R. J. Cava, and M. Z. Hasan, A topological Dirac insulator in a quantum spin Hall phase, Nature (London) **452**, 970 (2008).

[2] D. Hsieh, Y. Xia, D. Qian, L. Wray, J. Dil, F. Meier, J. Osterwalder, L. Patthey, J. Checkelsky, and N. P. Ong, A tunable topological insulator in the spin helical Dirac transport regime, Nature (London) **460**, 1101 (2009).

[3] B. A. Bernevig, T. L. Hughes, and S.-C. Zhang, Quantum spin Hall effect and topological phase transition in HgTe quantum wells, Science **314**, 1757 (2006).

[4] Y. Chen, J. G. Analytis, J.-H. Chu, Z. Liu, S.-K. Mo, X.-L. Qi, H. Zhang, D. Lu, X. Dai, and Z. Fang, Experimental realization of a three-dimensional topological insulator, Bi_2Te_3, Science **325**, 178 (2009).

[5] Y. Tokura, K. Yasuda, and A. Tsukazaki, Magnetic topological insulators, Nature Rev. Phys. **1**, 126 (2019).

[6] Y. Chen, J.-H. Chu, J. Analytis, Z. Liu, K. Igarashi, H.-H. Kuo, X. Qi, S.-K. Mo, R. Moore, and D. Lu, Massive Dirac fermion on the surface of a magnetically doped topological insulator, Science **329**, 659 (2010).

[7] H.-Z. Lu, W.-Y. Shan, W. Yao, Q. Niu, and S.-Q. Shen, Massive Dirac fermions and spin physics in an ultrathin film of topological insulator, Phys. Rev. B **81**, 115407 (2010).

[8] C.-Z. Chang, J. Zhang, X. Feng, J. Shen, Z. Zhang, M. Guo, K. Li, Y. Ou, P. Wei, and L.-L. Wang, Experimental observation of the quantum anomalous Hall effect in a magnetic topological insulator, Science **340**, 167 (2013).

[9] C.-Z. Chang, W. Zhao, D. Y. Kim, H. Zhang, B. A. Assaf, D. Heiman, S.-C. Zhang, C. Liu, M. H. Chan, and J. S. Moodera, High-precision realization of robust quantum anomalous Hall state in a hard ferromagnetic topological insulator, Nat. Mater. **14**, 473 (2015).

[10] J. Zhang, C.-Z. Chang, Z. Zhang, J. Wen, X. Feng, K. Li, M. Liu, K. He, L. Wang, and X. Chen, Band structure engineering in $(Bi_{1-x}Sb_x)_2Te_3$ ternary topological insulators, Nat. Commun. **2**, 574 (2011).

[11] J. Sánchez-Barriga, A. Varykhalov, G. Springholz, H. Steiner, R. Kirchschlager, G. Bauer, O. Caha, E. Schierle, E. Weschke, and A. Ünal, Nonmagnetic band gap at the Dirac point of the magnetic topological insulator $(Bi_{1-x}Mn_x)_2Se_3$, Nat. Commun. **7**, 10559 (2016).

[12] D. Zhang, A. Richardella, D. W. Rench, S.-Y. Xu, A. Kandala, T. C. Flanagan, H. Beidenkopf, A. L. Yeats, B. B. Buckley, and P. V. Klimov, Interplay between ferromagnetism, surface states, and quantum corrections in a magnetically doped topological insulator, Phys. Rev. B **86**, 205127 (2012).

[13] W. Zhao, D. Cortie, L. Chen, Z. Li, Z. Yue, and X. Wang, Quantum oscillations in iron-doped single crystals of the topological insulator Sb_2Te_3, Phys. Rev. B **99**, 165133 (2019).

[14] Y. Song, F. Yang, M.-Y. Yao, F. Zhu, L. Miao, J.-P. Xu, M.-X. Wang, H. Li, X. Yao, and F. Ji, Large magnetic moment of gadolinium substituted topological insulator: $Bi_{1.98}Gd_{0.02}Se_3$, Appl. Phys. Lett. **100**, 242403 (2012).

[15] S. Harrison, L. J. Collins-McIntyre, P. Schönherr, A. Vailionis, V. Srot, P. A. van Aken, A. Kellock, A. Pushp, S. Parkin, and J. Harris, Massive Dirac fermion observed in lanthanide-doped topological insulator thin films, Sci. Rep. **5**, 15767 (2015).

[16] L. Duffy, A. Frisk, D. Burn, N.-J. Steinke, J. Herrero-Martin, A. Ernst, G. van der Laan, and T. Hesjedal, Imposing long-range

ferromagnetic order in rare-earth-doped magnetic topological-insulator heterostructures, Phys. Rev. Mater. **2**, 054201 (2018).

[17] M. Li, C.-Z. Chang, L. Wu, J. Tao, W. Zhao, M. H. Chan, J. S. Moodera, J. Li, and Y. Zhu, Experimental Verification of the Van Vleck Nature of Long-Range Ferromagnetic Order in the Vanadium-Doped Three-Dimensional Topological Insulator Sb_2Te_3, Phys. Rev. Lett. **114**, 146802 (2015).

[18] Q. Liu, C.-X. Liu, C. Xu, X.-L. Qi, and S.-C. Zhang, Magnetic Impurities on the Surface of a Topological Insulator, Phys. Rev. Lett. **102**, 156603 (2009).

[19] G. C. Paul, S. F. Islam, P. Dutta, and A. Saha, Signatures of interfacial topological chiral modes via RKKY exchange interaction in Dirac and Weyl systems, Phys. Rev. B **103**, 115306 (2021).

[20] T. Chen, W. Liu, F. Zheng, M. Gao, X. Pan, G. van der Laan, X. Wang, Q. Zhang, F. Song, and B. Wang, High-mobility Sm-doped Bi_2Se_3 ferromagnetic topological insulators and robust exchange coupling, Adv. Mater. **27**, 4823 (2015).

[21] T. Yamasaki, K. Ueno, A. Tsukazaki, T. Fukumura, and M. Kawasaki, Observation of anomalous Hall effect in EuO epitaxial thin films grown by a pulse laser deposition, Appl. Phys. Lett. **98**, 082116 (2011).

[22] W. Branford, K. A. Yates, E. Barkhoudarov, J. Moore, K. Morrison, F. Magnus, Y. Miyoshi, P. Sousa, O. Conde, and A. J. Silvestre, Coexistence of Universal and Topological Anomalous Hall Effects in Metal CrO_2 Thin Films in the Dirty Limit, Phys. Rev. Lett. **102**, 227201 (2009).

[23] G. Kresse and J. Furthmuller, Phys. Rev. B **54**, 11169 (1996).

[24] A. I. Liechtenstein, V. I. Anisimov, and J. Zaane, Phys. Rev. B **52**, R5467(R) (1995).

[25] W. Zhao, L. Chen, Z. Yue, Z. Li, D. Cortie, M. Fuhrer, and X. Wang, Quantum oscillations of robust topological surface states up to 50 K in thick bulk-insulating topological insulator, npj Quantum Materials **4**, 56 (2019).

[26] A. Damascelli, Z. Hussain, and Z.-X. Shen, Angle-resolved photoemission studies of the cuprate superconductors, Rev. Mod. Phys. **75**, 473 (2003).

[27] S. Hüfner, *Photoelectron spectroscopy: Principles and applications* (Springer-Verlag, Berlin Heidelbery, 2013).

[28] M. Bianchi, R. C. Hatch, D. Guan, T. Planke, J. Mi, B. B. Iversen, and P. Hofmann, The electronic structure of clean and adsorbate-covered Bi_2Se_3: an angle-resolved photoemission study, Semicond. Sci. Technol. **27**, 124001 (2012).

[29] K. Kuroda, M. Arita, K. Miyamoto, M. Ye, J. Jiang, A. Kimura, E. Krasovskii, E. Chulkov, H. Iwasawa, and T. Okuda, Hexagonally Deformed Fermi Surface of the 3D Topological Insulator Bi_2Se_3, Phys. Rev. Lett. **105**, 076802 (2010).

[30] S.-Y. Xu, M. Neupane, C. Liu, D. Zhang, A. Richardella, L. A. Wray, N. Alidoust, M. Leandersson, T. Balasubramanian, and J. Sánchez-Barriga, Hedgehog spin texture and Berry's phase tuning in a magnetic topological insulator, Nat. Phys. **8**, 616 (2012).

[31] J. G. Analytis, R. D. McDonald, S. C. Riggs, J.-H. Chu, G. Boebinger, and I. R. Fisher, Two-dimensional surface state in the quantum limit of a topological insulator, Nat. Phys. **6**, 960 (2010).

[32] J. Choi, H.-W. Lee, B.-S. Kim, H. Park, S. Choi, S. Hong, and S. Cho, Magnetic and transport properties of Mn-doped Bi_2Se_3 and Sb_2Se_3, J. Magn. Magn. Mater. **304**, e164 (2006).

[33] See Supplemental Material at http://link.aps.org/supplemental/10.1103/PhysRevB.104.085153 for additional structural and transport properties of SFBS crystals.

[34] F. Tang, Y. Ren, P. Wang, R. Zhong, J. Schneeloch, S. A. Yang, K. Yang, P. A. Lee, G. Gu, and Z. Qiao, Three-dimensional quantum Hall effect and metal-insulator transition in $ZrTe_5$, Nature (London) **569**, 537 (2019).

[35] F.-X. Xiang, X.-L. Wang, M. Veldhorst, S.-X. Dou, and M. S. Fuhrer, Observation of topological transition of Fermi surface from a spindle torus to a torus in bulk Rashba spin-split BiTeCl, Phys. Rev. B **92**, 035123 (2015).

[36] K. Takiguchi, Y. K. Wakabayashi, H. Irie, Y. Krockenberger, T. Otsuka, H. Sawada, S. A. Nikolaev, H. Das, M. Tanaka, and Y. Taniyasu, Quantum transport evidence of Weyl fermions in an epitaxial ferromagnetic oxide, Nat. Commun. **11**, 4969 (2020).

[37] H.-Z. Lu, J. Shi, and S.-Q. Shen, Competition Between Weak Localization and Antilocalization in Topological Surface States, Phys. Rev. Lett. **107**, 076801 (2011).